A Universal Grey-Box High-Frequency Model for Calculating Bearing Voltage under WBG Inverter Drives Considering Frequency-Dependent Effects

Yue Yu, Hujun Peng, Simon Steentjes

***Abstract*—The integration of wide-bandgap (WBG) semiconductors in modern drive systems has significantly increased electrical stress on motor bearings due to ultra-high voltage slew rates (dv/dt). While conventional capacitive-divider models fail to capture the resulting high-frequency transients, this paper proposes a Universal High-Frequency Grey-Box Model that explicitly accounts for the frequency-dependent behavior of the winding, shaft, and bearing. Unlike existing methods, the proposed model incorporates a physically-grounded lubricant-film substructure that captures the transition from metallic contact at standstill to full-film lubrication under rotation, including the effects of oil bleeding and layer separation. Validation on a 40-kW PMSM test bench driven by a Silicon Carbide (SiC) inverter demonstrates that the model maintains an average relative peak-voltage error of 8.81% across 0 to 500 rpm. With a spectral correlation coefficient of 0.93, the framework provides a robust foundation for predicting localized electrical stress and lubricant degradation in high-speed, high-frequency power electronic drives.**

***Index Terms*—Bearing Voltage, Grey-Box Model, High-frequency modeling, Permanent Magnet Synchronous Machine, Transient overvoltage, Test bench**

I. Introduction

In modern industrial drive systems, bearing faults represent a major challenge for the reliable operation and maintenance of electrical machines. Statistical analyses indicate that more than 50% of machine failures are directly associated with bearing-related issues [1]. Further investigations have shown that, in inverter-fed drives in particular, Electric Discharge Machining (EDM) is one of the most critical mechanisms leading to premature bearing degradation [2]–[4]. EDM is initiated when the instantaneous bearing voltage becomes sufficiently high to exceed the dielectric breakdown threshold of the lubricant film that insulates the rolling elements from the raceways, causing the film to be punctured and a sharp discharge to occur [5], [6]. This discharge causes severe bearing damage, including bearing fluting and deteriorated lubricant, thereby shortening the equipment lifetime and compromising operational safety [7]–[9].

The bearing voltage, defined as the potential difference between the shaft end and the machine housing [10], can be classically estimated using the analytical expression of the so-called Bearing Voltage Ratio (BVR), as given by [11]:

$$\mathrm{BVR} = \frac{U_\mathrm{b}}{U_\mathrm{CM}} = \frac{C_\mathrm{wr}}{C_\mathrm{wr} + C_\mathrm{rf} + 2C_\mathrm{b}} \tag{1}$$

Y. Yu, H. Peng and S. Steentjes are associated with the Institute of Electrical Machines (IEM), RWTH Aachen University, Aachen, Germany. Corresponding authors are Y. Yu and H. Peng.

where U_b and U_CM denote the bearing voltage and Common-Mode (CM) voltage, C_wr and C_rf are the winding–rotor and rotor–frame capacitances, and C_b is the bearing capacitance, assuming identical Drive-End (DE) and Nonedrive-End (NDE) values with $C_\mathrm{b,DE} = C_\mathrm{b,NDE} = C_\mathrm{b}$. On this basis, the conventional bearing-voltage model in [11] considers only the effect of the nonzero common-mode voltage and represents the bearing voltage by a simplified capacitive divider. [12], [13] further develop the voltage-divider concept by formulating purely capacitive impedance networks aligned with the powertrain's mechanical geometry. In particular, [12] derives the network from the transmission assembly, whereas [13] builds a purely capacitive equivalent circuit reflecting the bearing construction. However, both approaches neglect frequency-dependent winding-related coupling on the bearing voltage. While such simplifications may be acceptable for basic analysis, these approaches become insufficient for studying bearing voltage in modern electrical drive systems, especially those intensified by the use of power modules based on wide-bandgap (WBG) semiconductors such as SiC and GaN MOSFETs, which operate with significantly higher switching frequencies and voltage slew rates [14]. The characteristics of WBG devices render the frequency-dependent Electromagnetic Interference (EMI) during machine operation non-negligible, intensifying terminal-voltage oscillations as well as the CM voltage, thereby potentially accelerating bearing degradation [15], [16]. As pointed out in [17], [18] indicate that adopting WBG devices can aggravate terminal-voltage overshoot and ringing, thereby increasing insulation stress and bearing-current stress. Moreover, [19] reported that, compared with Si-based inverters, SiC-based inverters increase the peak bearing discharge voltage by an average of 8.2% over the temperature range of 35–60 °C. When the temperature exceeds 55 °C, the voltage increase surpasses 10%–15%, leading to higher discharge energy. Weibull analysis of experimental

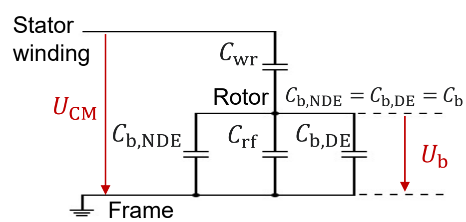

Fig. 1. Classical equivalent circuit for the determination of the BVR [11].

This article has been accepted for publication in IEEE Transactions on Power Electronics. This is the author's version which has not been fully edited and content may change prior to final publication. Citation information: DOI 10.1109/TPEL.2026.3688990

EDM events shows that above $55\,^{\circ}\mathrm{C}$, the SiC-based inverter exhibits an average 12% reduction in the Weibull shape parameter relative to the Si-based inverter, indicating a more dispersed voltage distribution and an increased probability of EDM over a wider bearing-voltage range. Further studies indicate that the elevated discharge energy associated with WBG inverters can locally raise the bearing temperature beyond the solidus temperature of bearing steel (approximately $1350\,^{\circ}\mathrm{C}$), thereby causing bearing damage [19]. In addition to localized thermal effects, variations in the electric field within the lubricant film can alter its chemical composition, leading to reduced viscosity and accelerated bearing degradation [20]. [21] shows the lubricant aging is approximately proportional to the oscillation frequency of the bearing voltage and current. Therefore, the frequency-dependent characteristics of the bearing, winding, and insulation system must be considered in bearing-voltage modeling to accurately capture voltage waveforms and peak values, which is critical for predictive maintenance and improved electrical machine design.

The so-called high-frequency modeling technique employs an equivalent circuit to characterize the frequency-dependent behavior of components under PWM electrical excitation. The reliability of this approach has been demonstrated in predicting terminal voltages and winding voltage distributions in electrical machines under WBG device [22], [23]. In recent years, several studies have applied high-frequency modeling approaches to describe and analyze the bearing voltage phenomena in electrical machines. In [24], a voltage-divider model is developed by incorporating the bearing structure into the winding model. However, the bearing representation in this work is overly simplified, as it includes only lumped parasitic capacitance and resistance, and the proposed model is not validated on a test bench under realistic operating conditions. Subsequent studies in [25], [26] further incorporate the inductive behavior of the bearing and shaft, while [27] proposes an improved bearing model that additionally captures high-frequency bearing behavior, circulating bearing currents, and current paths associated with EDM. Nevertheless, in all of these studies, the influence of the stator winding and its frequency-dependent impedance on the bearing voltage is still neglected.

To address these limitations, several high-frequency bearing models have been proposed that aim to better capture winding-induced frequency-dependent effects on bearing voltage. In [28], a high-frequency bearing model coupled with the machine winding is implemented to account for inductive effects; however, the model focuses mainly on the shaft and transmission, and the capacitive voltage across the bearing is neglected. Another bearing-voltage model in [29] is validated by impedance measurements, yet it does not explicitly capture the speed-dependent variation of the lubricant-film parasitic capacitance. Moreover, both studies lack time-domain validation on a test bench. In a related approach, [30] presents a simplified model based on frequency-band responses to predict the frequency-dependent bearing voltage; however, it has not been validated on an inverter-fed experimental setup under realistic operating conditions, and its bearing-voltage prediction accuracy therefore remains limited.

In view of the above limitations, the novelty of this work lies in establishing a physically structured grey-box framework that links impedance-based identification with time-domain bearing-voltage prediction in inverter-fed machines. The main contributions of this work are summarized as follows:

- A universal high-frequency grey-box model for bearing-voltage prediction is proposed. It is integrated with a validated high-frequency winding model to guarantee accurate terminal-voltage representation, which serves as the foundation of the overall modeling framework.
- Based on time-domain measurements of the terminal voltage and current, the transfer relationship between the terminal and bearing voltages is inversely identified and used for parameter optimization, yielding an accurate bearing submodel.
- The proposed model accounts for the frequency-dependent properties of the shaft, frame, and bearing, as well as parasitic phenomena within the bearing and the insulation system.
- With the ability to capture the frequency-dependent bearing-voltage behavior up to $10\,\mathrm{MHz}$, the model is extended from 0 to 500 rpm at $80\,^{\circ}\mathrm{C}$, since bearing-voltage variations beyond this range are marginal for machines of comparable power levels [31].
- Over the entire experimental speed range, the predicted peak bearing voltage exhibits an absolute error below 0.31 V. At standstill (0 rpm), the absolute and relative errors are 0.08 V and 13.58%, respectively, while for rotating conditions between 100 and 500 rpm the average absolute and relative errors are 0.24 V and 8.81%.
- The model faithfully reproduces the bearing-voltage profile, as evidenced by an average Pearson correlation coefficient of 0.93 between the modeled and measured bearing-voltage spectra.

While validated here on a 40-kW PMSM, the proposed universal framework builds on a high-frequency stator-winding model previously validated for different machine topologies [23], [32] and on a capacitive coupling structure common to both induction machines and PMSMs [6]. The remainder of this paper is organized as follows: Section II presents the impedance and time-domain bearing-voltage measurements on the PMSM test bench. Section III introduces the proposed high-frequency model and the parameter-identification procedure. Section IV gives the validation results and compares the proposed model with the conventional BVR-based model. Finally, Section V concludes the paper and outlines future work.

II. Measurements in the Frequency and Time Domains

The machine used in this study is a 40-kW PMSM, which features a single-tooth winding with eight pole pairs and twenty-four slots. Each of the U, V, and W phases consists of four parallel branches, where each branch comprises two coils connected in series, resulting in four neutral points in total. The following section presents the details of the impedance measurements in the frequency domain and the

This article has been accepted for publication in IEEE Transactions on Power Electronics. This is the author's version which has not been fully edited and content may change prior to final publication. Citation information: DOI 10.1109/TPEL.2026.3688990

voltage measurements on the test bench in the time domain, which together form the foundation of the proposed grey-box model.

A. Impulse Excitation Test for Assessing Rotational-Speed Influence on Bearing Voltage

According to the high-frequency modeling framework, the influence of rotational speed on the bearing-voltage response must be clarified before the main measurement campaign. In particular, it is necessary to determine the speed range over which the transient response remains sufficiently consistent.

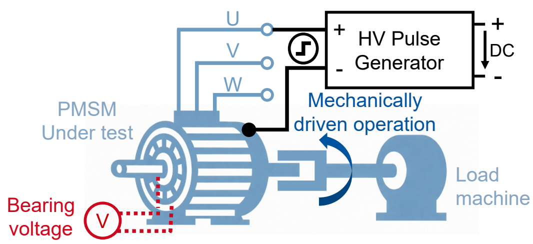

Fig. 2. Measurement setup for assessing rotational-speed influence.

To address this question, an impulse excitation test was conducted prior to the main measurements. Fig. 2 shows the experimental setup. In this experiment, the PMSM under test was mechanically driven by the load machine while being electrically separated from the cable and inverter, thereby minimizing electromagnetic interference. To ensure thermal conditions comparable to those of the subsequent measurements under inverter operation, the housing temperature was maintained at approximately 80 °C by water cooling. A high-frequency voltage pulse was applied between terminal U and the machine frame using an impulse generator. The pulse amplitude was 100 V and the slew rate was approximately 30 kV/μs, i.e., about twice the dv/dt of the inverter used on the test bench. The resulting bearing-voltage transient was measured at different rotational speeds.

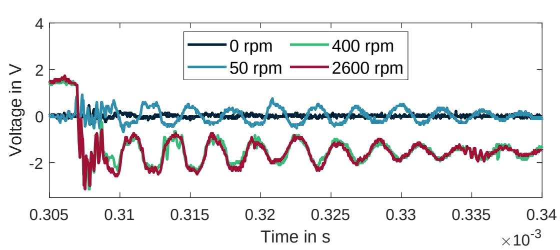

Fig. 3. Measured bearing-voltage waveforms under impulse excitation at different rotational speeds.

Fig. 3 shows the measured bearing-voltage transients for several representative rotational speeds. Only minor variations can be observed once the speed exceeds approximately 400 rpm, indicating that the transient response becomes largely stable in this range. This trend is further summarized in Fig. 4. The peak bearing voltage increases rapidly at low speeds and then gradually approaches a nearly constant value. Meanwhile, the Pearson correlation coefficient between successive transient waveforms exceeds 0.85 above approximately

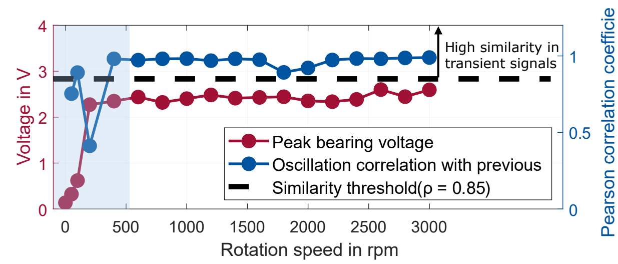

Fig. 4. Influence of rotational speed on the impulse-excited bearing-voltage response, characterized by the peak voltage and the Pearson correlation of successive transients.

500 rpm, indicating a high waveform similarity. These results suggest that the dominant bearing-voltage dynamics are only weakly affected by further speed increase beyond this range. Therefore, limiting the validation range of the proposed model to 500 rpm is justified.

B. Impedance Measurement in the Frequency Domain

Previous studies have shown that the bearing voltage is highly correlated with the CM voltage [10], [11]. Therefore, even with the inclusion of the bearing model, the overall machine model must still accurately capture the dynamics of the three-phase terminal voltages. As noted in [22], [33], the modeling approach based on CM and Differential-Mode (DM) impedances is an effective way to satisfy this fundamental premise. The impedance measurements were performed following the topologies summarized in Table I, by using a Keysight E4990A impedance analyzer over a frequency range of 100 Hz to 10 MHz. To avoid environmental interference, the measurements were carried out on the test bench with the machine. As reported in [34], [35], the rotor position has a negligible impact on terminal-voltage modeling. Therefore, all measurements were performed with the machine at standstill. Fig. 5 shows the measured CM and DM impedances. The ability to reproduce these impedance characteristics is essential for ensuring the accuracy of the overall model.

TABLE I
TOPOLOGIES FOR MEASURING THE IMPEDANCE SPECTRA OF THE PMSM.

Category	**Example**	**Impedance Between a Phase Terminal and**
Common-Mode	U–Frame	Frame
Differential-Mode	U–V	Another Phase Terminal

C. Time-Domain Measurement Setup and Signal Characterization

The classical impedance-based modeling approaches can not be applied for high-frequency modeling of machine bearing due to following reasons:

1) Impedance measurements can only be performed using two fixed contact points. When the shaft rotates, the contact points used to measure the bearing voltage change, making the impedance measurement results unreliable.

This article has been accepted for publication in IEEE Transactions on Power Electronics. This is the author's version which has not been fully edited and content may change prior to final publication. Citation information: DOI 10.1109/TPEL.2026.3688990

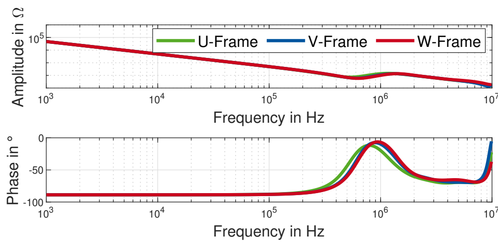

(a)

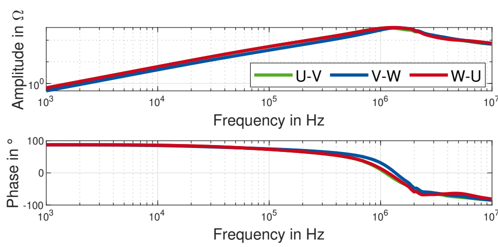

(b)

Fig. 5. Measured impedance magnitude and phase as functions of frequency for different connection topologies on on the test bench from 1 kHz to 10 MHz: (a) CM-Impedance, (b) DM-Impedance.

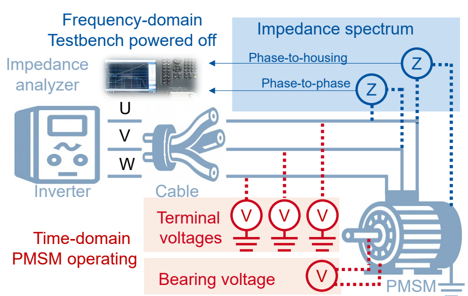

(a)

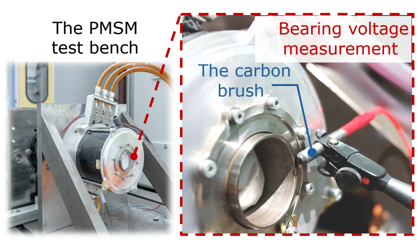

(b)

Fig. 6. Experimental setup for bearing voltage measurement on an operating PMSM: (a) test bench layout, (b) bearing voltage acquisition.

2) A rotating machine generates non-negligible bearing voltages. Conducting impedance measurements under rotation may damage the measuring instrument.

Therefore, modeling the bearing voltage under real operating conditions requires time-domain voltage measurements directly on the test bench.

*1) **Test Bench Configuration**:* Fig. 6a shows the test-bench setup. The PMSM is supplied by a SiC power-module-integrated inverter through a three-phase cable set. The machine housing and cable shield are bonded to ground. The voltages of the three machine terminals U, V, and W with respect to the frame are measured using active differential probes with bandwidth 25 MHz and are used directly as model inputs, i.e., without any filtering in the preprocessing stage. In practical implementations, these terminal voltages do not necessarily have to be measured directly. Instead, the machine-side terminal transients may be reconstructed using a suitable high-frequency model of the inverter–cable–machine system. In this context, the DC-link voltage together with the inverter switching states or PWM commands can provide an inverter-side excitation description, while the corresponding switching transients and voltage slew rates can be reproduced using inverter models that represent the switching behavior of the power devices, as commonly adopted in high-frequency transient simulations [33], [36]. However, such information is not sufficient by itself for bearing-voltage analysis and must be combined with an appropriate high-frequency representation of the cable and stator winding to obtain the terminal voltages relevant to the present study. As shown in Fig. 6b, the bearing voltage between the NDE and the machine frame was measured using a carbon brush, in accordance with the measurement method reported in [37]. To maintain relatively stable lubrication properties, the machine temperature was controlled at approximately 80 °C using a water-cooled housing, which this is close to the commonly referenced upper bound of the typical operating temperature for rolling bearings by Standard ISO 5593 [38]. And as reported in [31], at this temperature, the measured bearing voltage exhibits only marginal variation for rotational speeds above 500 rpm for machines operating at a comparable power level. Additionally, prolonged friction and machine losses (e.g., iron/copper) can rapidly increase bearing temperature via heat transfer [39]. For instance, 15 °C rise within 1 s at 1000 rpm was reported [39]. This changes lubricant viscosity and bleeding rate [40], affecting the its electrical characteristics [31]. Hence, the machine was stopped between speed tests to limit lubricant heating and keep thermal conditions consistent.

*2) **Excitation Bandwidth of the Measured Terminal Voltages**:* Fig. 7 shows the measured terminal-to-frame voltages at the machine terminals U, V, and W during inverter operation. As seen from the detailed waveform in Fig. 7b, each switching event excites a damped high-frequency transient at the machine terminals. To determine the relevant excitation bandwidth for the subsequent analysis, the spectral energy distribution of the measured terminal voltages is evaluated, as shown in Fig. 8. It can be observed that the dominant spectral components are concentrated below 10 MHz. On average, the spectral energy above 10 MHz accounts for only about 0.3% of the total signal energy. Hence, frequency components beyond 10 MHz are considered to have only a minor influence on the dominant transient behavior addressed in this work.

This observation is consistent with the theoretical bandwidth of the inverter switching transient. For the same SiC inverter platform, rise and fall times of $t_r = 51\,\text{ns}$ and $t_f = 26\,\text{ns}$ have been reported in [36]. Based on the commonly used estimate

$$f_{\text{co}} = \frac{1}{\pi \cdot \min(t_r, t_f)}, \tag{2}$$

a cutoff frequency of approximately 12.24 MHz is obtained.

This article has been accepted for publication in IEEE Transactions on Power Electronics. This is the author's version which has not been fully edited and content may change prior to final publication. Citation information: DOI 10.1109/TPEL.2026.3688990

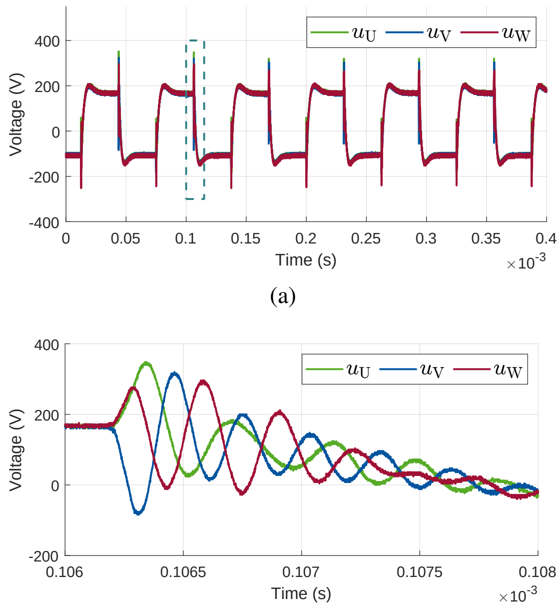

Fig. 7. Measured voltages of the three machine terminals U, V, and W with respect to the frame: (a) overview of the measured waveform; (b) detailed view of a representative switching transient.

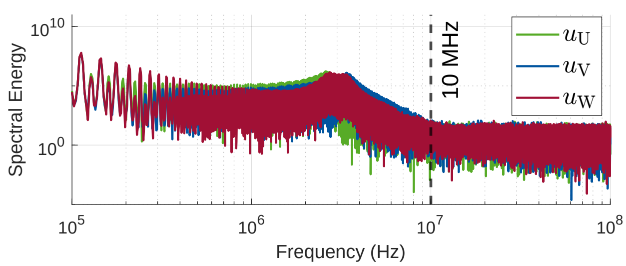

Fig. 8. Spectral energy distribution of the measured terminal voltages. More than 99.7% of the total spectral energy is located below 10 MHz.

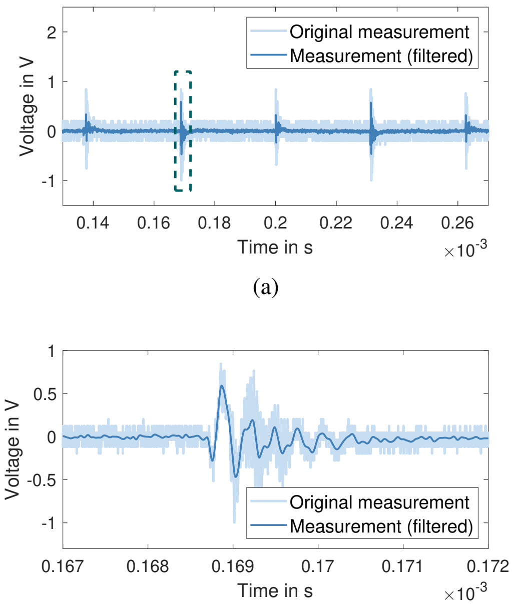

Fig. 9. Original and filtered bearing-voltage measurement at 0 rpm: (a) overall measurement, (b) detailed signal profile during the transient.

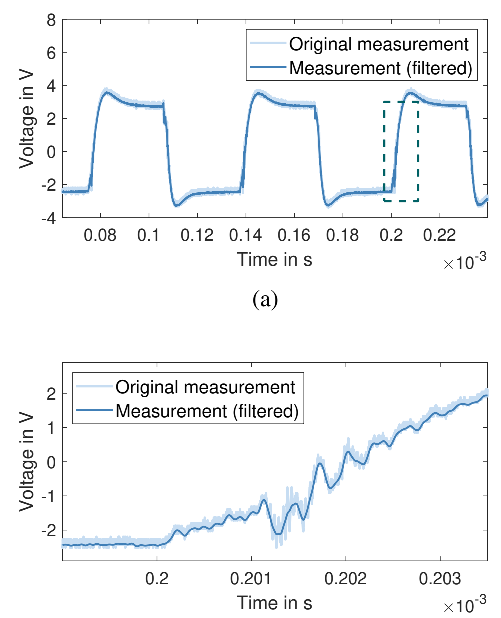

Fig. 10. Original and filtered bearing-voltage measurement at 500 rpm: (a) overall measurement, (b) detailed signal profile during the transient.

Although this cutoff frequency does not represent a strict spectral boundary, it indicates that the relevant excitation bandwidth lies in the order of several megahertz to about 10 MHz. Together with the measured energy distribution, this indicates that a model bandwidth of 10 MHz is sufficient to capture the dominant transient behavior considered in the present study.

*3) **Measured Bearing Voltage Waveforms**:* Fig. 9 and Fig. 10 show examples of the bearing-voltage waveforms at 0 rpm and 500 rpm, respectively. Since the measurements contain ultra–high-frequency noise above 10 MHz due to EMI, the terminal and bearing voltages are processed using a Fast Fourier Transform (FFT)-based filtering method. Frequency components exceeding 10 MHz are set to zero, and the inverse FFT is applied to reconstruct the signals, thereby preserving all spectral content below 10 MHz.

The conclusions regarding lubrication regimes reported in [41] help explain the differences observed between the two profiles. At 0 rpm, the bearing operates in boundary lubrication, and direct metal contact between the raceways and balls effectively shorts the lubricant-film capacitance. Thus, the circumferential voltage settles near zero after the switching-induced transient. Moreover, two adjacent transients within the same oscillation period (time spacing 0.0625 ms at 8 kHz) produce different bearing-voltage profiles due to asymmetric three-phase terminal overvoltage oscillations, indicating that the winding frequency dependence must be integrated into the bearing model. As the rotational speed increases, a full lubricant film develops, eliminating metallic contact. The combined influence of the non-zero CM voltage and the parasitic capacitance of the lubricant film produces a bearing voltage

This article has been accepted for publication in IEEE Transactions on Power Electronics. This is the author's version which has not been fully edited and content may change prior to final publication. Citation information: DOI 10.1109/TPEL.2026.3688990

profile that resembles a superposition of transient oscillations and a square wave. The detailed bearing-voltage waveforms are presented in Fig. 9b and Fig. 10b. The measurement results show that, when the electric drive system employs a WBG power module with a high slew rate, the resulting transient behavior produces significant oscillations in the bearing voltage that cannot be overlooked.

D. Frequency-Dependent Bearing Voltage Ratio

The definition of the BVR is given in (1) as the ratio of bearing voltage to CM voltage, based on a capacitive voltage divider model illustrated in Fig. 1. In classical high-frequency modeling, the system is typically assumed to be a Linear Time-Invariant (LTI) system. The frequency-dependent impedance is then recognized as Frequency Response Functions (FRFs), which describe the dynamic response behavior of system components. A similar approach is adopted in this study to analyze bearing behavior. Based on Eq.(1), the BVR is defined as the FRF from the CM voltage to the bearing voltage, expressed as:

$$\mathrm{BVR}(\mathrm{j}\omega) = \frac{U_{\mathbf{b}}(\mathrm{j}\omega)}{U_{\mathbf{CM}}(\mathrm{j}\omega)} \tag{3}$$

where the time-domain signal is transformed into the frequency domain using the Fourier transform:

$$X(\mathrm{j}\omega) = \int_{-\infty}^{\infty} x(t)e^{-\mathrm{j}\omega t}\mathrm{d}t \tag{4}$$

$\mathrm{BVR}(\mathrm{j}\omega)$ can be transformed into a frequency-based representation $\mathrm{BVR}(\mathrm{j}\omega)$ as follows:

$$\mathrm{BVR}(f) = \mathrm{BVR}(\mathrm{j}\omega)\big|_{\omega=2\pi f} \tag{5}$$

This representation allows the bearing voltage ratio to be presented in the form of a frequency spectrum. Fig. 11 shows the calculated $\mathrm{BVR}(f)$ spectrum at 500 rpm. Above 100 kHz, the transfer characteristic from the CM voltage to the bearing voltage exhibits a clear frequency dependence. This property should not be overlooked when modeling the dynamic behavior of bearing voltage, particularly in capturing voltage profiles associated with transient oscillations induced by high voltage slew rates. The frequency-dependent BVR shown in Fig. 11 therefore serves as a direct motivation for the development of the bearing model presented in the next section. The basic model, illustrated in Fig. 1 as a simple voltage divider, lacks the capability to capture frequency-dependent dynamics and to provide a detailed description of the lubricant film and bearing components. These limitations will be addressed in the next section.

III. Grey-Box Modeling Approach of Bearing Voltage

A. Model Overview

Fig. 12 illustrates the proposed grey-box model, which extends the model in [22]. To capture the frequency-dependent behavior of the stator winding under high-frequency voltage excitation, the winding is conceptually divided into two branches, accounting for parasitic capacitances as well as skin

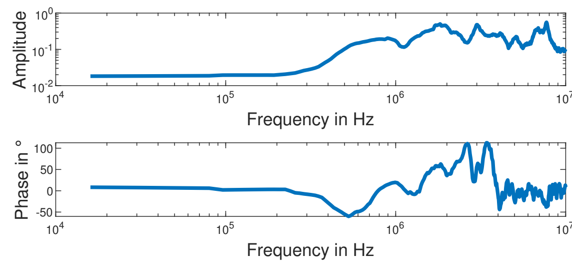

Fig. 11. Calculated BVR magnitude and phase as functions of frequency at 500 rpm.

and proximity effects. In [22], all remaining machine parts except the stator winding were simplified as a zero-potential node, and the insulation path was represented by a series RC circuit. For bearing-voltage analysis, however, this part must be modeled in more detail. Therefore, two structurally identical subsystems, connected to different winding nodes, are introduced to represent the insulation paths between the winding and the stator frame, and between the winding and the shaft. The corresponding equivalent circuit is shown in Fig. 13: a large resistor models the insulation resistance, a capacitor the parasitic capacitance, and an additional RC branch the frequency-dependent dielectric losses. As indicated in Fig. 12,

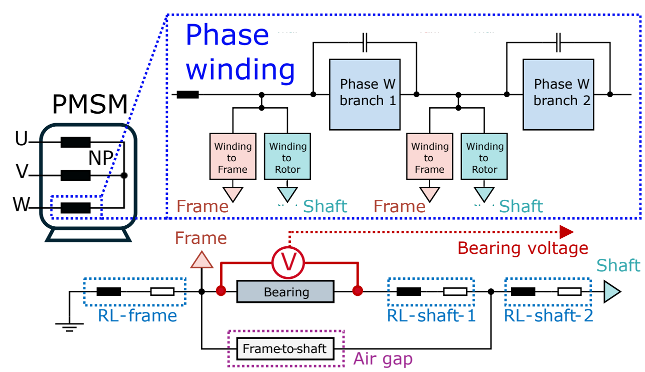

Fig. 12. Overview of a the grey-box winding model integrated with the bearing structure.

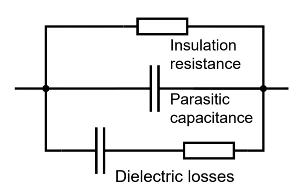

Fig. 13. Model structure of the insulation layer and air gap.

the individual paths between the winding and the frame or shaft, formed by the parasitic circuits, are abstracted as point-to-point circuits. However, by modeling the bearing voltage, the skin effect of the stator frame and the shaft themselves should not be neglected. Considering the shaft and frame as metallic conductors, the skin effect dominates their frequency-dependent behavior. As frequency f increases, the alternating

This article has been accepted for publication in IEEE Transactions on Power Electronics. This is the author's version which has not been fully edited and content may change prior to final publication. Citation information: DOI 10.1109/TPEL.2026.3688990

current concentrates near the conductor surface, characterized by the *skin depth* δ [42]:

$$\delta = \sqrt{\frac{1}{2\pi f \mu \sigma}} \tag{6}$$

where σ is the conductor conductivity, μ is the magnetic permeability. The reduced skin depth decreases the effective conduction area, thereby increasing the effective resistance and decreasing the internal inductance. As shown in [42], for a solid cylindrical copper conductor, the resistance increases monotonically with frequency, while the internal inductance asymptotically approaches zero. This behavior is modeled by the classical RL ladder network in Fig. 14, which stacks RL series elements with increasing resistance in successive layers [43]. As shown in Fig. 12, the stator frame is represented by this structure labeled with 'RL-frame', with one end fixed at zero potential to represent grounding to the machine housing. For the shaft, the parasitic paths between the frame and the shaft, as well as those between the winding and the shaft, cannot be simplified as converging at a single point. Therefore, two segmented RL ladder networks 'RL-shaft-1' and 'RL-shaft-2' are used to represent different sections of the shaft. In addition, the air gap between the frame and the shaft is treated as a dielectric and is modeled using the same structure shown in Fig. 13. The bearing model substructure is connected between the ungrounded end of the 'RL-frame' subsystem and 'RL-shaft-1'.

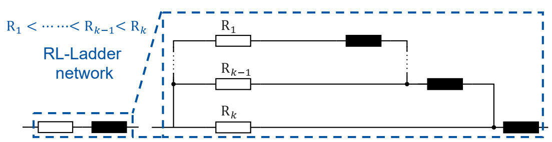

Fig. 14. Example of an RL ladder network for modeling the skin effect.

B. *Structure of the Ball-Bearing Model*

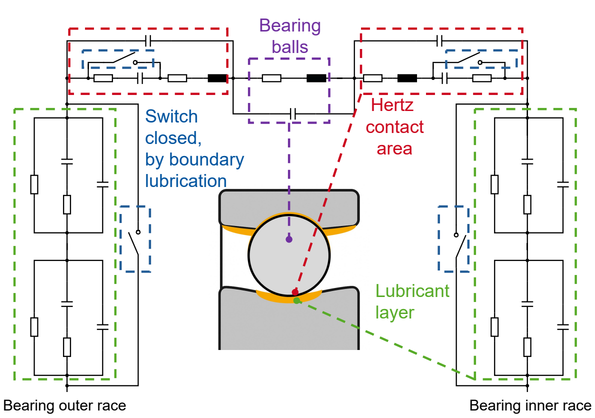

Fig. 15. Model structure of a rolling bearing considering the frequency-dependent characteristics of the bearing balls and lubricant film with the boundary-lubrication switch.

Based on the grey-box modeling concept, the DE and NDE bearings are represented by identical subsystems and combined to form the overall bearing model. Fig. 15 illustrates the structure of the bearing model. In the central branch of this equivalent circuit, an RL-ladder network is introduced to represent the skin effect of the bearing balls acting as metallic conductors, analogous to the shaft modeling approach described in Section III-A. A small-valued capacitor is connected in parallel to account for the parasitic capacitance in the air surrounding the bearing balls.

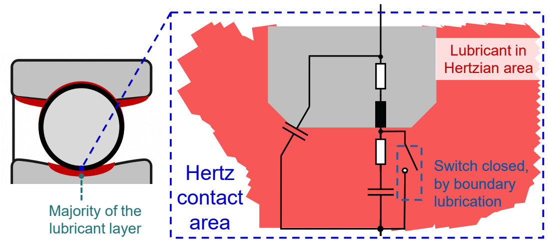

Fig. 16. Detail of the bearing contact model: equivalent circuit of the Hertzian contact, illustrating the impact of oil bleeding on the lubricant-film impedance.

In previous studies, when analyzing a single bearing ball, the Hertzian contact area with elastic deformation is typically taken as the only corresponding electrode area for the bearing current conduction path [11]. However, in the high-frequency range, the effective conductive area in this region decreases due to the skin effect. In addition, when metallic contact occurs under boundary lubrication near the Hertzian contact region, the distance between the bearing balls and races becomes extremely small, resulting in relatively high parasitic capacitance. Currents may therefore flow through this parasitic path, which can be regarded as equivalently present even under full-film lubrication. a new structure is introduced, as shown in Fig 16. The overall conductive behavior of the bearing balls is represented by an RL-ladder network, which captures the frequency-dependent reduction of the effective conductive cross-section. In series with this network, a low-magnitude resistor and a high-magnitude capacitor are included to represent the electrical properties of the ultra-thin lubricant layer in the Hertzian area. A switch bypasses this RC series branch when purely metallic contact occurs between the balls and the races. In addition, an extra capacitor is connected in parallel with the entire structure to account for the parasitic capacitance in the lubricant or air gap at the edge of the Hertzian contact region. Based on the assumption that the lubricant layer properties vary with rotational speed, these resistance and capacitance values in this branch are treated as speed-dependent. The lubricant layer is modeled, analogous

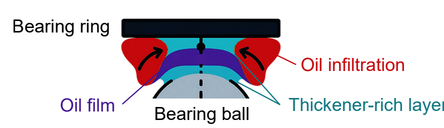

Fig. 17. Schematic of oil bleeding and layer separation in lubricant film [40].

to the insulation system described in Section III-A, using a three-branch parallel RC network. These branches respectively capture the lubricant's conductive resistance, parasitic capacitance, and dielectric losses. As illustrated in Fig. 17, a typical

This article has been accepted for publication in IEEE Transactions on Power Electronics. This is the author's version which has not been fully edited and content may change prior to final publication. Citation information: DOI 10.1109/TPEL.2026.3688990

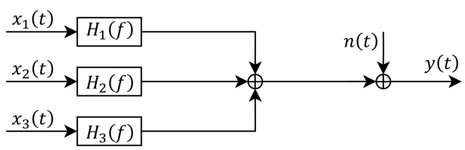

Fig. 18. Three-input/single-output system with noise on the output for H_1 estimator.

grease is a two-phase system composed of a base oil and a thickener in stationary status. The thickener forms a sponge-like network that retains the base oil and enables its gradual migration toward the rolling contact region. When the rolling element passes through this region, the local contact pressure expels the infiltrated oil from the thickener matrix, forming so-called bleeding oil, which provides effective lubrication to the contact interface [40]. Due to the distinct frequency-dependent electrical properties of the base-oil film and the thickener-rich layer, the lubricant layer is represented by a two-layer series structure in the proposed model. Furthermore, a switch connected in parallel to the lubricant layer is introduced to model the standstill condition of the bearing, in which a metallic contact forms between the bearing balls and the raceways. It should be emphasized that, due to the intrinsic dependence of the lubricant layer properties and on bearing clearance on rotational speed, the rotation-speed dependency of the model is captured through the variation of the lubricant-related parameters.

C. Parameter Identification

The parameter identification process is formulated as a dual-condition optimization problem, with objectives defined under Condition 1 and Condition 2:

- **Condition 1** Reproduction of CM/DM impedance spectra for insulation accuracy.
- **Condition 2** Accurate transfer relationship from the three terminal voltages to the bearing voltage.

Based on Condition 1, the FRF spectrum generated by the model must match the impedance spectra measured in Sec. II-B, following the methodology described in [22].

To satisfy Condition 2, the time-domain measurements in Fig. 6a are separated into the three inputs $u_{\mathrm{U}}(t)$, $u_{\mathrm{V}}(t)$, $u_{\mathrm{W}}(t)$, and the output $u_{\mathrm{B}}(t)$, from which the input–output transfer relationship is must be identified. Due to the high DC-link voltage at the inverter, the input voltages exceed $130\,\mathrm{V}$ and exhibit significant overvoltage oscillations, while the resulting bearing voltage remains below $4\,\mathrm{V}$. Under these measurement conditions, the Signal-to-Noise Ratio (SNR) of the terminal voltages as inputs is much lower than that of the bearing voltage as output, especially at $0\,\mathrm{rpm}$, where the average SNR of the input signals is $35.1\,\mathrm{dB}$, whereas the output signal exhibits an SNR of only $1.28\,\mathrm{dB}$. Therefore, assuming the system is LTI, the H_1 estimator is employed to compute the FRFs from the terminal voltages to the bearing voltage [44].

Fig. 18 illustrates the system structure suitable for the H_1 estimator in a 3-input/1-output configuration, with $x_1(t)$, $x_2(t)$, and $x_3(t)$ as inputs and $y(t)$ as the output. The additional contaminating noise $n(t)$ is assumed to arise only from the output measurement. After all time-domain signals are transformed and projected onto the corresponding frequencies via the Discrete Fourier Transform (DFT), in frequency f the output signal $Y \in \mathbb{C}$ can be expressed in matrix form as:

$$\begin{aligned} &Y = \mathbf{H}\mathbf{X} + N \quad \text{with} \quad N \in \mathbb{C}. \\ &\mathbf{X} = [X_1\ X_2\ X_3]^\top \in \mathbb{C}^{3\times1}, \quad \mathbf{H} = [H_1\ H_2\ H_3] \in \mathbb{C}^{1\times3} \end{aligned} \tag{7}$$

where $\mathbf{X}$ denotes the input vector, $\mathbf{H}$ represents the frequency response vector, and N is the measurement noise. In the system identification problem, $\mathbf{H}$ is considered unknown and is estimated via complex least squares as

$$\hat{\mathbf{H}} = \arg\min_{\mathbf{H}} \|Y - \mathbf{H}\mathbf{X}\|_2^2, \tag{8}$$

with residual $Y - \hat{\mathbf{H}}\mathbf{X} \approx N$. The least squares solution is obtained by left-multiplying the system equation by the Hermitian transpose of the input and then taking the expectation of each term:

$$\mathbf{X}^H Y = \mathbf{X}^H \mathbf{H}\mathbf{X} + \mathbf{X}^H N. \tag{9}$$

The measurement record is first segmented using a fixed-length moving window, whose length is chosen sufficiently large so that the time-domain signals within each window can be regarded as approximately wide-sense stationary. Under this assumption, by evaluating the signals at each frequency f, (9) can be reformulated in terms of ensemble expectations as:

$$\mathbb{E}[\mathbf{X}^H Y] = \mathbb{E}[\mathbf{X}^H \mathbf{H}\mathbf{X}] + \mathbb{E}[\mathbf{X}^H N]. \tag{10}$$

The system noise is assumed to originate entirely from the output measurement and uncorrelated with the input signals:

$$\mathbb{E}[\mathbf{X}^H N] = 0. \tag{11}$$

Substituting this result into (10) yields

$$\mathbb{E}[\mathbf{X}^H Y] = \mathbb{E}[\mathbf{X}^H \mathbf{H}\mathbf{X}]. \tag{12}$$

Taking the Hermitian transpose of both sides of (12) and using $(\mathbb{E}[Z])^H = \mathbb{E}[Z^H]$ gives

$$\mathbb{E}[Y^* \mathbf{X}] = \mathbb{E}[\mathbf{X}\mathbf{X}^H]\,\mathbf{H}^H. \tag{13}$$

Then taking the Hermitian transpose of (13) and exploiting the Hermitian property of the auto-correlation matrix yields

$$\mathbb{E}[Y\mathbf{X}^H] = \mathbf{H}\,\mathbb{E}[\mathbf{X}\mathbf{X}^H]. \tag{14}$$

According to the standard definition of correlation matrices, $\mathbb{E}[Y\mathbf{X}^H]$ and $\mathbb{E}[\mathbf{X}\mathbf{X}^H]$ in (14) can be written as the cross-correlation and auto-correlation matrices, denoted by $\mathbf{G}_{\mathrm{YX}}$ and $\mathbf{G}_{\mathrm{XX}}$, respectively [45]:

$$\mathbb{E}[\mathbf{X}\mathbf{X}^H] = \left[\mathbb{E}[X_i X_j^*]\right]_{i,j=1}^3 = \mathbf{G}_{\mathrm{XX}} \tag{15}$$

$$\mathbb{E}[Y\mathbf{X}^H] = \left[\mathbb{E}[YX_1^*]\ \mathbb{E}[YX_2^*]\ \mathbb{E}[YX_3^*]\right] = \mathbf{G}_{\mathrm{YX}} \tag{16}$$

$$\mathbb{E}[Y\mathbf{X}^H] = \left[\mathbb{E}[YX_1^*] \quad \mathbb{E}[YX_2^*] \quad \mathbb{E}[YX_3^*]\right] = \mathbf{G}_{\mathrm{YX}} \tag{17}$$

Substituting (15) and (17) into (14) yields

$$\mathbf{G}_{\mathrm{YX}} = \mathbf{H}\,\mathbf{G}_{\mathrm{XX}}. \tag{18}$$

This article has been accepted for publication in IEEE Transactions on Power Electronics. This is the author's version which has not been fully edited and content may change prior to final publication. Citation information: DOI 10.1109/TPEL.2026.3688990

Finally, the frequency-response vector $\mathbf{H}$ at frequency f is given by

$$\mathbf{H} = \mathbf{G}_{\mathrm{YX}}\,\mathbf{G}_{\mathrm{XX}}^{-1}. \tag{19}$$

In the parameter identification procedure, the terminal voltages $u_{\mathrm{U}}(t)$, $u_{\mathrm{V}}(t)$, and $u_{\mathrm{W}}(t)$, along with the bearing voltage $u_{\mathrm{B,meas}}(t)$, are assigned to the system variables as $x_1(t)$, $x_2(t)$, $x_3(t)$, and $y_1(t)$, respectively. The frequency response vector, calculated according to (19), is then assembled across the entire frequency range, thereby yielding the FRF from the terminal voltages to the bearing voltage:

$$\mathbf{H}_{\mathrm{meas}}(\mathrm{j}\boldsymbol{\omega}) = \begin{bmatrix} H_{\mathrm{U}}(\mathrm{j}\boldsymbol{\omega}) & H_{\mathrm{V}}(\mathrm{j}\boldsymbol{\omega}) & H_{\mathrm{W}}(\mathrm{j}\boldsymbol{\omega}) \end{bmatrix}^{\top}, \tag{20}$$

where $\boldsymbol{\omega} = \left[2\pi f_0,\, 2\cdot 2\pi f_0,\, \dots\right]$ and f_0 denotes the fundamental DFT frequency resolution.

Since the input excitation does not cover the full frequency range, directly comparing the analytical FRF extracted from the model with the measured $\mathbf{H}_{\mathrm{meas}}(\mathrm{j}\omega)$ would introduce bias. Therefore, the same input signals are applied to the model to obtain the modeled output $u_{\mathrm{B,model}}(t)$, and $\mathbf{H}_{\mathrm{model}}(\mathrm{j}\omega)$ is computed from $u_{\mathrm{B,model}}(t)$ using the same procedure. Finally, the optimization objective becomes

$$\min_{\boldsymbol{\theta}}\ J(\boldsymbol{\theta}) = \sum_{k=1}^{K} \left\| \mathbf{H}_{\mathrm{meas}}(\mathrm{j}\omega_k) - \mathbf{H}_{\mathrm{model}}(\mathrm{j}\omega_k;\boldsymbol{\theta}) \right\|_2^2, \tag{21}$$

where $\boldsymbol{\theta}$ denotes the vector of model parameters.

The initial parameter identification is based on the impedance measurements and the time-domain measurements acquired at zero rotational speed, both of which correspond to the same operating status. Satisfying both Condition 1 and Condition 2 under these circumstances ensures that the model can simultaneously predict the terminal voltages accurately and identify the bearing-related parameters in the standstill state. Subsequently, while keeping all other parameters fixed, the optimization problem defined in (21) is solved by treating the lubricant-related parameters as design variables, thereby obtaining the model parameters that reflect the rotational-speed-dependent variations of the lubricant layer properties.

IV. Results

A. Model validation based on test bench measurements

The model's ability to accurately reproduce the terminal voltage is verified by the model's consistency with themeasured impedance spectrum. Fig. 19 presents the example of measured and modeled CM and DM impedance spectra, showing agreement from 1 kHz to 10 MHz. Table II summarizes the statistical evaluation results. In addition to the Mean Absolute Percentage Error (MAPE), the Coherence Coefficient introduced in [22] is employed to assess the modeling accuracy. This metric quantifies the consistency between two system responses subjected to identical excitation across frequencies, ranging from 0 to 1, with 1 indicating perfect correlation. As shown in Table II, the model achieves an average relative error of 6.43% across all impedance spectra and an average Coherence Coefficient of 0.99682. These results confirm that the model accurately reproduces the impedance characteristics, thereby ensuring reliable prediction of the terminal voltage

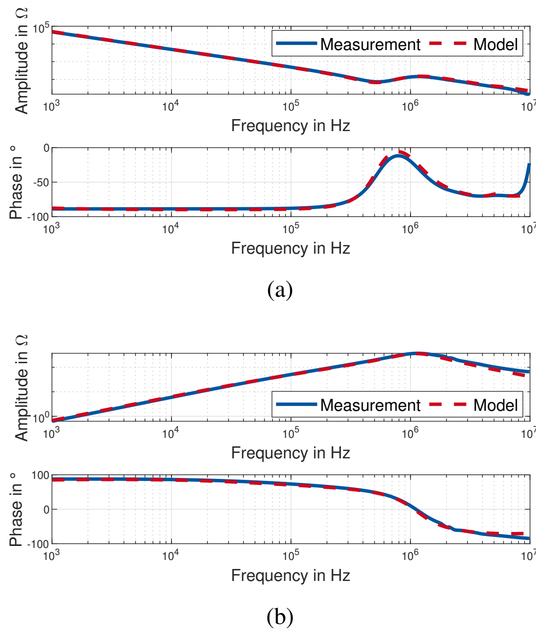

Fig. 19. The modeled and measured impedance on the test bench from 1 kHz to 10 MHz: (a) U-Frame (CM), (b) U-V(DM).

TABLE II
STATISTICAL VALIDATION RESULTS USING THE MEASURED IMPEDANCE SPECTRUM FROM 1 kHz TO 10 MHz.

Measurement topology	MAPE (%)	Coherence Coefficient
U–Frame	6.4429	0.9995
V–Frame	4.5457	0.9989
W–Frame	7.0750	0.9994
U–V	7.9125	0.9951
V–W	5.9611	0.9932
W–U	6.5435	0.9948

while also providing a basis for extending the model toward the analysis of motor ground leakage current.

Fig. 20 presents the overview and detailed validation results based on the test-bench measurements of bearing voltage at 0 rpm, where a purely metallic contact exists between the bearing balls and races, and the parasitic capacitance is effectively short-circuited through this conductive path. During the stationary interval between two transient events, the bearing and shaft are essentially grounded to the machine frame, resulting in a bearing voltage of zero. However, the transient behavior induces noticeable oscillations in the bearing voltage, with a peak magnitude of approximately 0.6 V. The proposed model accurately reproduces this behavior, yielding an absolute peak-voltage prediction error of only 0.08 V, and the simulated oscillation waveform closely matches the measured profile.

As described in Section II, increasing the speed from 0 to 500 rpm enhances lubrication and eliminates metallic contact, thereby altering the electrical properties of the lubricant film. Under this condition, the switches in Fig. 15 and Fig. 16 remain open, such that the resistance and parasitic capacitance of the lubricant film dominate the high-frequency behavior. As the speed increases, although the electrical properties of the thickener-rich film are not yet understood, the entire lubricant film becomes thicker and exhibits layer separation due to oil bleeding. Consequently, the parasitic capacitance of the entire

This article has been accepted for publication in IEEE Transactions on Power Electronics. This is the author's version which has not been fully edited and content may change prior to final publication. Citation information: DOI 10.1109/TPEL.2026.3688990

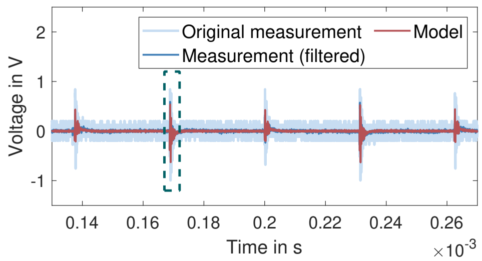

(a)

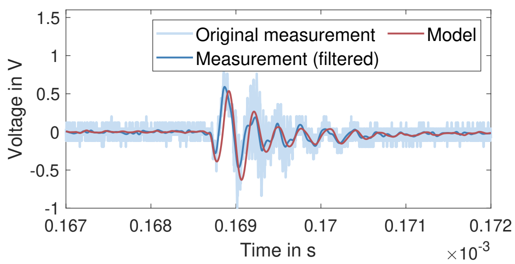

(b)

Fig. 20. Time-domain validation using test bench bearing-voltage measurement at 0 rpm: (a) overall, (b) detailed signal profile during the transient.

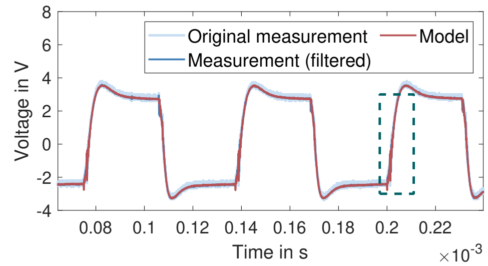

(a)

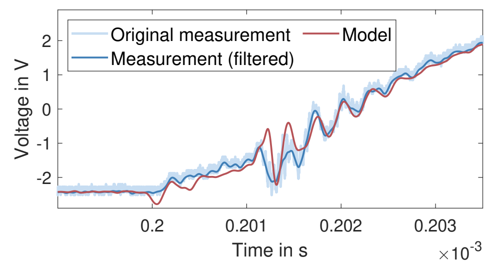

(b)

Fig. 22. Time-domain validation using test bench bearing-voltage measurement at 500 rpm: (a) overall, (b) detailed signal profile during the transient.

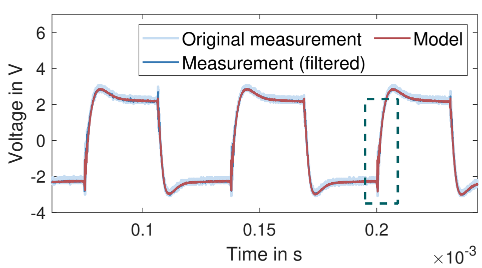

(a)

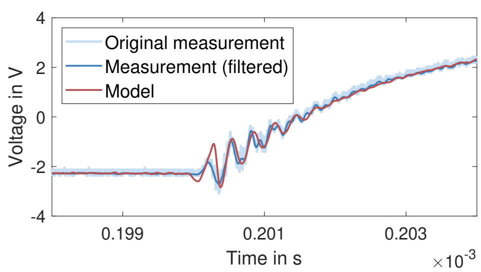

(b)

Fig. 21. Time-domain validation using test bench bearing-voltage measurement at 100 rpm: (a) overall, (b) detailed signal profiles during the transient.

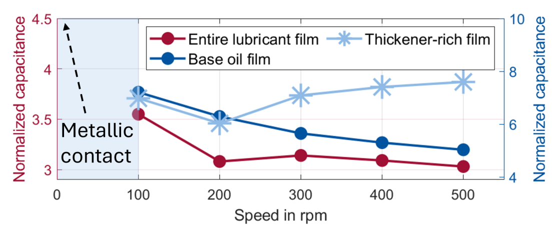

(a)

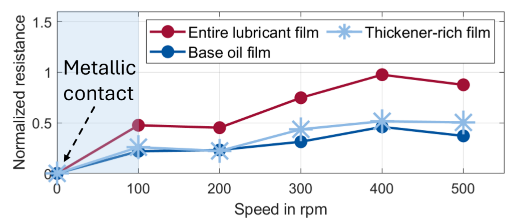

(b)

Fig. 23. Variation of lubricant-film equivalent model parameters as a function of rotational speed (a) equivalent resistance, (b) equivalent capacitance.

lubricant layer decreases, whereas the resistance associated with its insulating behavior increases. These overall trends are consistently reflected in the equivalent lubricant-related parameters extracted from the model at different speeds, as shown in Fig. 21. Fig. 22 and Fig. 23 present the validation results obtained from test bench bearing-voltage measurements at 100 rpm and 500 rpm, respectively. The model accurately predicts the peak bearing-voltage values and effectively captures the oscillatory behavior induced by the transient excitation.

To quantitatively assess the accuracy of the model, the absolute and relative errors of the predicted peak bearing voltage are calculated and summarized in Table III. From 0 rpm to 500 rpm, the model consistently maintains an absolute prediction error below 0.31 V. At 0 rpm, where lubricant-film effects can be neglected and purely metallic contact occurs between the bearing balls and races, the absolute error is only 0.08 V. The corresponding relative error (13.58%) is higher mainly because the standstill peak voltage is small, which amplifies percentage errors. Notably, the absolute error is minimal at 0 rpm, indicating high physical fidelity under the simplest contact condition. Under all other operating

This article has been accepted for publication in IEEE Transactions on Power Electronics. This is the author's version which has not been fully edited and content may change prior to final publication. Citation information: DOI 10.1109/TPEL.2026.3688990

TABLE III
VALIDATION RESULTS BEARING VOLTAGE MODELING AT DIFFERENT ROTATIONAL SPEEDS.

Speed (rpm)	Absolute Error (V)	Relative Error (%)	Coherence Coefficient of Spectrum Distribution
0	0.08	13.56	0.9080
100	0.30	11.58	0.9658
200	0.29	9.70	0.9022
300	0.12	3.81	0.9597
400	0.22	6.71	0.9422
500	0.30	12.30	0.9281

TABLE IV
STATISTICS OF PARAMETERS IN THE CONVENTIONAL BEARING VOLTAGE MODEL.

C_{wr} (pF)	C_{rf} (pF)	Speed (rpm)	Average BVR (%)	Calculated C_{b} (nF)
637	1287	0	0.007	- (upper limit)
		100	1.620	18.1

conditions, the model achieves an average absolute error of $0.24\,\mathrm{V}$ and an average relative error of 8.81%.

In addition to time-domain validation using the bearing-voltage signal, frequency-domain analysis is performed by computing the spectra of the measured and simulated bearing-voltage signals at each rotational speed. Following the method in [22], spectral correlation coefficients are calculated for all operating speeds and summarized in Table III. The coefficients range from 0.9022 to 0.9658, with values close to unity indicating strong spectral agreement, demonstrating that the proposed model accurately captures the dominant frequency-domain characteristics of the measured bearing-voltage signals under various operating conditions.

B. Comparison between the proposed model and conventional bearing voltage model

To highlight the importance of frequency-dependent effects and component behavior in bearing-voltage analysis, this section compares the proposed model with the conventional model in [11]. Fig. 1 shows the structure of the conventional model. The common-mode voltage U_{com}, used as the model input, is calculated as follows:

$$U_{\mathrm{com}}(t) = \frac{U_{\mathrm{U}}(t) + U_{\mathrm{V}}(t) + U_{\mathrm{W}}(t)}{3} \tag{22}$$

The parasitic capacitances C_{wr} and C_{rf}, representing the winding-to-frame and winding-to-rotor capacitances, are estimated from the simulated impedances of the corresponding parts in the proposed grey-box model. The parasitic capacitance inside the bearing is assumed as in [11]: $C_{\mathrm{b,NDE}} = C_{\mathrm{b,DE}} = C_{\mathrm{b}}$. This indicates that both bearings at either end of the shaft exhibit identical parasitic capacitance. Finally, the value of C_{b} is determined using the procedure described in Section III-C, yielding the values at 0 rpm and 100 rpm, respectively. Table IV summarizes the parameters of the conventional bearing voltage model. Fig. 24 presents the comparison at 0 rpm. The traditional model considers only the parasitic capacitance between the winding and the bearing and does not account for the possibility of metallic contact in the boundary-lubricant regime. This deficiency, together with the nearly zero average BVR listed in Table IV, drives the optimization to an unrealistically large value of C_{b} in the traditional model, which in turn indicates a conductive path in the equivalent circuit. As a result, it fails to reproduce the oscillatory bearing-voltage transients generated during switching events. Under boundary-lubrication conditions—typically occurring at low rotational speeds or under insufficient lubrication—these oscillations dominate the dynamic behavior of the bearing voltage and therefore must not be neglected, as they directly determine the peak voltage applied across the bearing and influence the likelihood of electrical discharge. The proposed model incorporates this effect and successfully captures the characteristic transient oscillations, achieving a markedly improved agreement with the measurement.

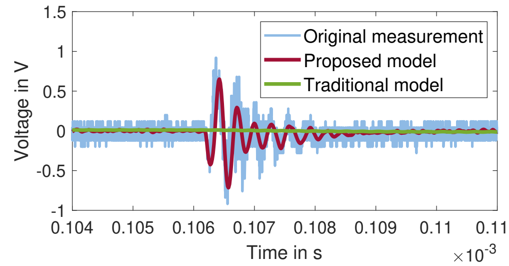

Fig. 24. Comparison of bearing-voltage prediction between the traditional model and the proposed model at 0 rpm during the transient.

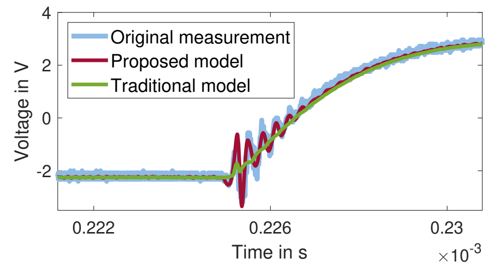

Fig. 25. Comparison of bearing-voltage prediction between the traditional model and the proposed model at 100 rpm during the transient.

Fig. 25 presents the comparison at 100 rpm. Although the traditional model reproduces the overall trend, it cannot capture the switching-induced oscillations because the capacitive-divider structure neglects the frequency-dependent behavior of the winding and the bearing. As shown in Fig. 25, the measured peak bearing voltage at 100 rpm is about $3.04\,\mathrm{V}$. The proposed model predicts $2.77\,\mathrm{V}$, corresponding to a relative error of 8.9%, whereas the traditional model predicts only about $2.15\,\mathrm{V}$, resulting in a relative error of 29.3%. This comparison highlights the importance of incorporating frequency-dependent effects in bearing-voltage prediction.

Moreover, the significance of reproducing the transient oscillations goes beyond peak-value prediction. The electrical stress across the bearing is not determined by the peak voltage alone; the oscillation frequency, damping behavior, and local waveform shape also affect the likelihood of lubricant-film breakdown, electrical discharge, and the resulting bearing degradation [7], [19], [21]. In particular, the transient oscillations govern how the voltage is distributed across the lubricant film over time, thereby influencing the local electric-field stress and repeated high-frequency excitation. Such oscillatory voltages can also cause localized temperature rises within the lubricating film, which may accelerate grease decomposition and degradation [20]. Therefore, even when a conventional model happens to match the peak voltage in a specific case, its inability to represent the oscillatory dynamics still limits its physical interpretability and predictive capability under high-frequency inverter operation.

Beyond the comparison with the classical capacitive-divider model, several recent bearing-voltage models have also introduced important extensions. The model in [24] relies on static capacitance-based bearing parameters, whereas [25], [26] include inductive shaft–bearing effects but still use static-capacitance-based winding representations. Hence, the frequency-dependent bearing dynamics under fast switching transients are not fully captured. The models in [28]–[30] further improve specific aspects, but they still rely on simplified or static-FEM-derived representations and therefore do not provide a unified description of speed-dependent lubricant-film behavior and frequency-dependent bearing dynamics under inverter-fed operation. In contrast, the proposed model combines a physically structured lubricant-film submodel with an independently validated high-frequency stator-winding model, enabling the coupled frequency-dependent behavior of the winding, shaft, frame, and bearing to be captured within one grey-box framework. In addition, the grey-box formulation avoids repeated FEM-based derivations, uses accessible parameters, and keeps the computational effort moderate through a linear frequency-domain network representation.

V. Conclusion

This work introduces a universal grey-box high-frequency model designed for the accurate prediction of bearing voltages in inverter-fed electrical machines. By integrating a high-frequency winding model with a detailed bearing substructure, the proposed approach captures the complex transient dynamics induced by modern power electronics. The model explicitly accounts for the frequency-dependent characteristics of the shaft, frame, and bearing components, alongside the parasitic effects inherent to the insulation system.

A key contribution of this research is the incorporation of rotational speed effects—specifically lubricating film thickness and grease bleeding—into the model structure. This enables a robust reproduction of speed-dependent impedance variations and ensures a physically consistent representation of the bearing's electrical response over a wide operating range. The parameter identification process, grounded in CM and DM impedance spectra from 1 kHz to 10 MHz and refined via time-domain measurements using an H_1 estimator, ensures both spectral and temporal fidelity. Validation on an SiC-inverter-fed PMSM test bench (0 to 500 rpm) demonstrates high predictive accuracy. The model successfully captures transient oscillations and peak voltage values, maintaining an absolute error below 0.31 V and an average relative error of 8.81% under rotating conditions. A Pearson correlation coefficient of 0.93 further confirms the model's ability to replicate dominant frequency-domain dynamics.

Compared to conventional BVR-based capacitive-divider models, this grey-box approach offers superior performance under the high voltage slew rates characteristic of WBG devices. It provides a quantitatively reliable and physically interpretable foundation for assessing bearing electrical stress. Future work will extend this framework into a multi-physics model by integrating temperature and vibration signals, validating it on additional machine and bearing types, and investigating the influence of dv/dt, ultimately supporting EDM prediction and predictive maintenance.

References

[1] M. A. Saleh, A. Ghrayeb, S. S. Refaat, H. Abu-Rub, S. P. Khatri, and J. Kammermann, "Attention-enhanced agru framework for induction motor incipient fault diagnosis in electric vehicles," *IEEE Transactions on Instrumentation and Measurement*, vol. 74, pp. 1–17, 2025.

[2] A. Binder and A. Muetze, "Scaling effects of inverter-induced bearing currents in AC machines," *IEEE Transactions on Industry Applications*, vol. 44, no. 3, 2008.

[3] Z. Xiao, M. Hu, S. Chen, and K. Cao, "Bearing electrical-erosion damage in electrical drive systems: A review," *IEEE Transactions on Transportation Electrification*, vol. 10, no. 2, pp. 3428–3442, 2024.

[4] F. He, G. Xie, and J. Luo, "Electrical bearing failures in electric vehicles," *Friction*, vol. 8, pp. 4–28, 2020.

[5] D. De Gaetano, W. Zhu, X. Sun, X. Chen, A. Griffo, and G. W. Jewell, "Experimental ball bearing impedance analysis under different speed and electrical conditions," *IEEE Transactions on Dielectrics and Electrical Insulation*, vol. 30, no. 3, pp. 1312–1321, 2023.

[6] A. Muetze, "Bearing currents in inverter-fed AC motors," Ph.D. dissertation, Technische Universität Darmstadt, Darmstadt, Germany, 2004.

[7] R. Collin, A. Yokochi, and A. von Jouanne, "EDM damage assessment and lifetime prediction of motor bearings driven by PWM inverters," in *Proceedings of the IEEE Energy Conversion Congress and Exposition (ECCE)*, Detroit, MI, USA, 2022, pp. 1–6.

[8] A. K. Morya, M. C. Gardner, B. Anvari, L. Liu, A. G. Yepes, J. Doval-Gandoy, and H. A. Toliyat, "Wide bandgap devices in ac electric drives: Opportunities and challenges," *IEEE Transactions on Transportation Electrification*, vol. 5, no. 1, pp. 3–20, 2019.

[9] M. Weicker and A. Binder, "Characteristic parameters for electrical bearing damage," in *Proceedings of the International Symposium on Power Electronics, Electrical Drives, Automation and Motion (SPEEDAM)*, Sorrento, Italy, 2022, pp. 785–790.

[10] T. Plazenet, T. Boileau, C. Caironi, and B. Nahid-Mobarakeh, "A comprehensive study on shaft voltages and bearing currents in rotating machines," *IEEE Transactions on Industry Applications*, vol. 54, no. 4, pp. 3749–3759, 2018.

[11] A. Muetze and A. Binder, "Calculation of motor capacitances for prediction of the voltage across the bearings in machines of inverter-based drive systems," *IEEE Transactions on Industry Applications*, vol. 43, no. 3, pp. 665–672, Jun. 2007.

[12] C. Huang, L. Xiong, D. Meng, M. Zhang, Y. Gong, and H. Guo, "Modeling and analysis of capacitive bearing voltage of in-wheel hub motor reduction system for electric vehicles," in *Proceedings of the IEEE International Conference on Power Science and Technology (ICPST)*, Kunming, China, 2025, pp. 1775–1779.

[13] Y. Feng, R. Ji, Z. Hong, J. Wang, J. Song, L. Gao, X. Hao, and J. Tan, "Analytical optimization of the bearing voltage of motor considering the thickness of insulating coating: An improved equivalent circuit model," *IEEE Sensors Journal*, vol. 22, no. 19, pp. 18 567–18 579, Oct. 2022.

[14] M. Buffolo, "Review and outlook on GaN and SiC power devices: Industrial state-of-the-art, applications, and perspectives," *IEEE Transactions on Electron Devices*, vol. 71, no. 3, pp. 1344–1355, Mar. 2024.

[15] H. Dai, R. A. Torres, T. M. Jahns, and B. Sarlioglu, "Comparative study of conducted common-mode EMI in WBG-enabled DC-fed three-phase current-source inverter," *IEEE Journal of Emerging and Selected Topics in Power Electronics*, vol. 10, no. 6, pp. 7188–7204, Dec. 2022.

[16] S. Yunus, W. Ming, and C. E. Ugalde-Loo, "Motor overvoltage mitigation using SiC-based zero-voltage switching inverter," *IEEE Transactions on Power Electronics*, vol. 39, no. 1, pp. 1195–1208, Jan. 2023.

[17] Y. Xu, Y. Liang, X. Yuan, X. Wu, and Y. Li, "Experimental assessment of high-frequency bearing currents in an induction motor driven by a SiC inverter," *IEEE Access*, vol. 9, pp. 40 540–40 549, 2021.

[18] Y. Azadeh, A. B. Mirza, and F. Luo, "Investigation of motor winding overvoltages in integrated WBG-based motor drive systems," in *Proceedings of the 2024 IEEE Applied Power Electronics Conference and Exposition (APEC)*, 2024, pp. 148–152.

[19] R. Collin, A. Yokochi, and A. von Jouanne, "Novel characterization of Si- and SiC-based PWM inverter bearing currents using probability density functions," in *Proceedings of the IEEE Energy Conversion Congress and Exposition (ECCE)*, Vancouver, BC, Canada, 2021, pp. 5146–5153.

[20] A. Romanenko, A. Muetze, and J. Ahola, "Effects of electrostatic discharges on bearing grease dielectric strength and composition," *IEEE Transactions on Industry Applications*, vol. 52, no. 6, pp. 4835–4842, 2016.

[21] J. Ahola, V. Särkimäki, A. Muetze, and J. Tamminen, "Radio-frequency-based detection of electrical discharge machining bearing currents," *IET Electric Power Applications*, vol. 5, no. 4, pp. 386–392, 2011.

[22] H. Peng, Y. Yu, S. Stevic, and S. Steentjes, "High-frequency modeling of electrical drive systems considering test bench environment influence," *IEEE Transactions on Power Electronics*, vol. 40, no. 9, pp. 12 816–12 828, Sep. 2025.

[23] H. Peng, Y. Yu, and K. Hameyer, "Conductor-based modeling of a single-tooth winding for EMI simulation," *IEEE Transactions on Power Electronics*, vol. 39, no. 9, pp. 11 099–11 109, 2024.

[24] P. Han, G. Heins, D. Patterson, M. Thiele, and D. M. Ionel, "Modeling of bearing voltage in electric machines based on electromagnetic FEA and measured bearing capacitance," *IEEE Transactions on Industry Applications*, vol. 57, no. 5, pp. 4765–4775, Sep. 2021.

[25] M. Asefi and J. Nazarzadeh, "A fast transient model for bearing fault analysis in induction machine drives," *IEEE Sensors Journal*, vol. 19, no. 5, pp. 1897–1904, Mar. 2019.

[26] S. Xiao, H. Li, Z. Zhan, G. Wu, Y. Cao, T. Li, X. Yan, J. Zeng, Q. Wang, Y. Pan, Y. Qian, G. Gao, Y. Guo, and X. Zhang, "Overvoltage-induced bearing corrosion in high-speed train traction motors: Analysis and mitigation," *Engineering Failure Analysis*, vol. 185, p. 110440, 2026.

[27] M. Jaritz, C. Jaeger, M. Bucher, J. Smajic, D. Vukovic, and S. Blume, "An improved model for circulating bearing currents in inverter-fed AC machines," in *Proceedings of the IEEE International Conference on Industrial Technology (ICIT)*, Melbourne, Australia, 2019, pp. 225–230.

[28] Y. Tombul, J. Zhang, and J. Andert, "High-frequency modeling of bearing and transmission currents in electric vehicles," in *Proceedings of the International Conference on Electrical Machines (ICEM)*, Torino, Italy, 2024, pp. 1–6.

[29] S. Quabeck, "Modeling of parasitic currents and fault detection in electrical traction drives," Ph.D. dissertation, Rheinisch-Westfälische Technische Hochschule Aachen (RWTH Aachen University), Aachen, Germany, 2023.

[30] M. Yea, J. Kim, and K. J. Han, "Frequency-dependent bearing voltage model for squirrel-cage induction motors," *IEEE Transactions on Industrial Electronics*, vol. 69, no. 5, pp. 5071–5080, May 2022.

[31] E. Wittek, M. Kriese, H. Tischmacher, S. Gattermann, B. Ponick, and G. Poll, "Capacitances and lubricant film thicknesses of motor bearings under different operating conditions," in *Proceedings of the XIX International Conference on Electrical Machines (ICEM 2010)*, 2010, pp. 1–6.

[32] H. Peng, Y. Yu, and S. Steentjes, "Universal modeling methods of induction machines to study the influence of rotor existence on terminal overvoltages during inverter-fed operation," in *2025 IEEE International Electric Machines & Drives Conference (IEMDC)*, 2025, pp. 157–163.

[33] M. Turzyński, "Induction machine behavioral modeling for prediction of emi propagation," *Bulletin of the Polish Academy of Sciences Technical Sciences*, vol. 65, no. No 2, pp. 247–254, 2017.

[34] H. Peng, Y. Yu, and S. Steentjes, "Universal modeling methods of induction machines to study the influence of rotor existence on terminal overvoltages during inverter-fed operation," in *Proceedings of the IEEE International Electric Machines and Drives Conference (IEMDC)*, Houston, TX, USA, 2025, pp. 157–163.

[35] D. Zhao, K. Shen, W. Liu, L. Lang, and P. Liang, "A measurement-based wide-frequency model for aircraft wound-rotor synchronous machine," *IEEE Transactions on Magnetics*, vol. 55, no. 7, pp. 1–8, 2019.

[36] S. Stevic, Y. Tombul, M. Lauerburg, A. Thul, and K. Hameyer, "Overvoltage transients in wide bandgap-based inverter-fed variable speed electrical drives," in *PCIM Europe 2022; International Exhibition and Conference for Power Electronics, Intelligent Motion, Renewable Energy and Energy Management*, 2022, pp. 1–9.

[37] Z. Li, R. Liu, Y. Hao, D. Zheng, and J. Gui, "A novel nonintrusive measurement method of bearing currents in inverter-fed motors," *IEEE Sensors Journal*, vol. 25, no. 19, pp. 36 580–36 593, 2025.

[38] *DIN ISO 5593:2024-08: Wälzlager—Begriffe (ISO 5593:2023); Rolling bearings—Vocabulary (ISO 5593:2023)*, DIN Std., Aug. 2024, 134 pp.

[39] Q. Ai, H. Wei, H. Dou, W. Zhao, and Y. Zhang, "Robust rotor temperature estimation of permanent magnet motors for electric vehicles," *IEEE Transactions on Vehicular Technology*, vol. 72, no. 7, pp. 8579–8591, 2023.

[40] S. Zhang, G. Jacobs, and P. M. Lugt, "Calculation of the lubricating film thickness in grease-lubricated rolling contacts," Ph.D. dissertation, RWTH Aachen University, Aachen, Germany, 2024.

[41] V. Schneider, C. Behrendt, P. Höltje, D. Cornel, F. M. Becker-Dombrowsky, S. Puchtler, F. Gutiérrez Guzmán, B. Ponick, G. Jacobs, and E. Kirchner, "Electrical bearing damage, a problem in the nano- and macro-range," *Lubricants*, vol. 10, no. 8, p. 194, Aug. 2022.

[42] O. M. O. Gatous and J. P. Filho, "A new formulation for skin-effect resistance and internal inductance frequency-dependent of a solid cylindrical conductor," in *Proceedings of the 2004 IEEE/PES Transmission and Distribution Conference and Exposition: Latin America*, 2004, pp. 919–924.

[43] N. Idir, Y. Weens, and J.-J. Franchaud, "Skin effect and dielectric loss models of power cables," *IEEE Transactions on Dielectrics and Electrical Insulation*, vol. 16, no. 1, pp. 147–154, 2009.

[44] A. Brandt, *Noise and Vibration Analysis*. John Wiley & Sons, 2011.

[45] J. A. Gubner, *Probability and Random Processes for Electrical and Computer Engineers*. USA: Cambridge University Press, 2006.